



Published in final edited form as:

Tomography. 2016 December ; 2(4): 260–266. doi:10.18383/j.tom.2016.00142.

Quantitative Magnetization Transfer Imaging of the Breast at 3.0 T: Reproducibility in Healthy Volunteers

Lori R. Arlinghaus¹, Richard D. Dortch^{1,2,3}, Jennifer G. Whisenant⁴, Hakmook Kang^{5,6}, Richard G. Abramson^{1,2,4}, and Thomas E. Yankeelov^{7,8,9,10}

¹Vanderbilt University Institute of Imaging Science, Vanderbilt University Medical Center, Nashville, Tennessee

²Department of Radiology and Radiological Sciences, Vanderbilt University Medical Center, Nashville, Tennessee

³Department of Biomedical Engineering, Vanderbilt University, Nashville, Tennessee

⁴Vanderbilt-Ingram Cancer Center, Vanderbilt University Medical Center, Nashville, Tennessee

⁵Department of Biostatistics, Vanderbilt University Medical Center, Nashville, Tennessee

⁶Center for Quantitative Sciences, Vanderbilt University Medical Center, Nashville, Tennessee

⁷Department of Biomedical Engineering, The University of Texas at Austin, Austin, Texas

⁸Department of Internal Medicine, The University of Texas at Austin, Austin, Texas

⁹Institute for Computational and Engineering Sciences, The University of Texas at Austin, Austin, Texas

¹⁰Livestrong Cancer Institutes, The University of Texas at Austin, Austin, Texas

Abstract

Quantitative magnetization transfer magnetic resonance imaging provides a means for indirectly detecting changes in the macromolecular content of tissue noninvasively. A potential application is the diagnosis and assessment of treatment response in breast cancer; however, before quantitative magnetization transfer imaging can be reliably used in such settings, the technique's reproducibility in healthy breast tissue must be established. Thus, this study aims to establish the reproducibility of the measurement of the macromolecular-to-free water proton pool size ratio (PSR) in healthy fibroglandular (FG) breast tissue. Thirteen women with no history of breast disease were scanned twice within a single scanning session, with repositioning between scans. Eleven women had appreciable FG tissue for test–retest measurements. Mean PSR values for the FG tissue ranged from 9.5% to 16.7%. The absolute value of the difference between 2 mean PSR measurements for each volunteer ranged from 0.1% to 2.1%. The 95% confidence interval for the mean difference was $\pm 0.75\%$, and the repeatability value was 2.39%. These results indicate that

This is an open access article under the CC BY 4.0 license (<https://creativecommons.org/licenses/by/4.0/>).

Corresponding Author: Lori R. Arlinghaus, PhD, Vanderbilt University Institute of Imaging Science, Vanderbilt University Medical Center, 1161 21st Avenue South, MCN AA-1101, Nashville, TN 37232-2310; lori.arlinghaus@vanderbilt.edu.

Disclosures: No disclosures to report.

Conflict of Interest: None reported.

the expected measurement variability would be $\pm 0.75\%$ for a cohort of a similar size and would be $\pm 2.39\%$ for an individual, suggesting that future studies of change in PSR in patients with breast cancer are feasible.

Keywords

quantitative MR; breast cancer; pool size ratio; test–retest

INTRODUCTION

Because of the complicated nature of tumors and their microenvironment (1), a variety of quantitative imaging techniques, each probing unique aspects of the tissue, are required to provide a more complete picture of the changes observed in both the diagnostic and prognostic settings. In addition, as the number of targeted cancer therapies increases (2), it is important to have corresponding imaging techniques that are sensitive to the specific changes induced by such therapies. Two major aspects of tumor physiology that have been studied clinically with magnetic resonance imaging (MRI) are tumor vasculature (3) and cellularity (4). Dynamic contrast-enhanced MRI (DCE-MRI) provides information related to tumor vasculature, making it useful for assessing antiangiogenic therapies, whereas diffusion-weighted MRI is sensitive to tumor cellularity, making it useful for assessing cytotoxic therapies. Recently, we reported that combining DCE-MRI and diffusion-weighted MRI measures increases the ability to predict breast cancer response to neoadjuvant therapy at a very early time point (5). However, although the measurements were relatively sensitive (92%), they were only modestly specific (78%), warranting investigation of other imaging parameters reflecting additional aspects of the tumor environment to more accurately predict treatment response.

Another aspect of the tumor environment that has recently gained increasing attention is the extracellular matrix (ECM) (6, 7). Once thought to be a passive medium, the ECM is now known to be involved in both tumor development and progression (1, 8, 9). The ECM comprises several glycoproteins, including collagen, laminin, proteoglycans, and fibronectin. Although the low concentration and fast relaxation of the protons of these macromolecules make them difficult to image directly with conventional MRI methods (because of their short T_2), their effects on free water can be explored via magnetization transfer MRI (MT-MRI) (10).

MT-MRI is sensitive to changes in the macromolecular content of tissue and takes advantage of the fact that macromolecular protons communicate their spin information to protons in the surrounding free water through dipole–dipole interactions and/or chemical exchange. The magnetization transfer (MT) effect is conventionally quantified by the MT ratio (MTR): $MTR = 1 - M_{\text{sat}}/M_0$, where M_{sat} is the MT-weighted image and M_0 is the reference image with no MT-weighting.

Initial applications of MT-MRI in breast cancer showed a significant reduction of MTR in malignancies compared with benign lesions (11, 12). Bonini et al. (11) hypothesized that increased proteolytic activity may cause a reduction of macromolecules in the malignant

tumor environment, thus resulting in reduced MTR. Furthermore, it has been shown that the concentration of collagen type I, the primary structural component of breast ECM, is reduced in the hypoxic tumor environment (13). ECM characteristics are known to change during the tumor life cycle and in response to treatment (14–16); thus, it is a reasonable hypothesis that the MTR may change during the course of therapy and potentially be useful for predicting treatment response. However, MTR measurements are sensitive to the experimental design, making longitudinal comparison difficult. More specifically, both the method of saturation of the macro-molecular proton pool (power, offset frequency, and duty cycle) and the image acquisition parameters (repetition time [TR], echo time [TE], and flip angle) affect the observed MTR values. In addition, MT-MRI is truly only a semiquantitative imaging technique, as MTR measurements are affected by both the relaxation and exchange rates of the free water and macromolecular proton pools. Therefore, a quantitative MT (qMT) approach is necessary to separate the contributions from MT and relaxation effects (17, 18) and, ideally, provide more specific information about tissue composition than the MTR.

Although reports of qMT imaging of tumors (19–23) and changes to the extracellular environment due to disease (23, 24) are limited, these efforts suggest that the macromolecular-to-free water proton pool size ratio (PSR) differs between healthy tissue and tumors or fibrotic tissue. We, therefore, hypothesize that the PSR of breast tumors, as measured with qMT, will be altered compared with the surrounding fibroglandular (FG) tissue and will change in response to successful therapy, potentially improving prediction of treatment response in an ongoing clinical trial (5). However, to assess the sensitivity of qMT imaging in treatment prognosis, an expectation of the variation in the PSR of healthy breast tissue is necessary. Thus, in this contribution, we sought to determine the reproducibility of PSR measurements of the breast in healthy controls.

METHODOLOGY

Subjects

Thirteen women with no history of breast disease were scanned twice within a single scanning session with a 5- to 10-minute break between scans, allowing the volunteers to stretch. Two volunteers did not have any appreciable FG tissue, leaving 11 data sets for analysis (ages: 25–54 years; mean: 33 years). Subjects were consented as part of a study approved by the local Institutional Review Board. Demographic data were collected and managed using REDCap (Research Electronic Data Capture) electronic data capture tools hosted at the Vanderbilt University (25).

Magnetic Resonance Imaging

Data were acquired with a 3.0 T Achieva MR scanner equipped with a 2-channel multitransmit body coil and a MammoTrak table that includes a dedicated 16-channel receive double-breast coil (Philips Healthcare, Best, The Netherlands). The Mammo-Trak table (Philips Healthcare, Best, The Netherlands) automatically places the breast coil at the magnet isocenter. Image-based radiofrequency (RF) and B_0 shimming were performed using the SmartBreast software package (Philips Healthcare, Best, The Netherlands).

For qMT imaging, an MT-prepared (20-milliseconds sinc-Gauss pulse), segmented echo planar imaging sequence (3-dimensional gradient echo with 5 lines/shot) with a water-selective excitation pulse (1-3-3-1 binomial, 6°), TR/TE = 48/6.6 milliseconds, sensitivity encoding factor = 1.5, flow-compensation, and respiratory gating was used. A sagittal volume was acquired with a field of view (FOV) = $256 \times 256 \times 50 \text{ mm}^3$, acquisition matrix = $128 \times 126 \times 10$ sections, and a reconstructed voxel size = $1.33 \times 1.33 \times 5 \text{ mm}^3$. This FOV was centered on the left breast, with an attempt to approximately match the stack placement between scan sessions. [Slice orientation, FOV, and voxel size were chosen to coordinate with those being acquired in an ongoing longitudinal, multiparametric study of response prediction in breast cancer (5).] Data were collected at 4 MT-offset frequencies (1, 2, 4 and 8 kHz) using 2 MT pulse angles (500° and 800°), plus 1 acquisition for normalization (offset frequency = 100 kHz and pulse angle = 800°), resulting in a total of 9 image volumes in a (minimum) scan time of 1 minute 38 seconds. (The actual scan time varied depending on the volunteer's respiration rate and was typically ~3 minutes.)

The qMT model requires independent T_1 , RF transmit (B_1^+), and main magnetic field (B_0) estimates. T_1 was estimated using the multiple flip angle method with 10 flip angles (2:2:20°), TR/TE = 7.9/4.6 milliseconds, and a matrix size of 192×192 with a 192×192 reconstruction. B_1^+ was measured using a Bloch–Siegert method (26), with TR/TE = 491/5.4 milliseconds and a matrix size of 104×102 with a 192×192 reconstruction. B_0 was measured using a dual-gradient echo method with fat and water protons in phase with TR/TE = 12/4.6 milliseconds and a matrix size of 84×85 with a 192×192 reconstruction. Each measurement was acquired with the same FOV as the qMT data ($256 \times 256 \times 50 \text{ mm}^3$) and 10 sections. Scan times for the multiple flip angle, B_1^+ , and B_0 maps were 1 minute 7 seconds, 1 minute 44 seconds, and 9 seconds, respectively.

Data Analysis

All data were nonrigidly coregistered to the normalization qMT image volume (Advanced Normalization Tools, Philadelphia, Pennsylvania). FG tissue volumes of interest (VOIs) were extracted from each reference qMT image volume in a semiautomated 3-step process (27). First, a threshold-binning procedure eliminated the background noise and voxels affected by partial-volume averaging. Next, the skin and chest wall were manually excluded from the VOI. Finally, the first and last sections were excluded to remove potential interpolation artifacts due to the image registration process.

The registered and masked data were fit to a 2-pool model to estimate PSR and the T_2 of the macromolecular protons (T_2^M) (28, 29). During fitting, the T_1/T_2 of water protons and the MT rate were fixed to the following published values in skeletal muscle: 40 and 48 Hz, respectively (29). This model reduction was necessary because the number of offsets/angles acquired was limited by the longer scan times associated with respiratory gating. Previous work using similar qMT model reduction strategies has shown that estimated PSR values are relatively insensitive to errors in the assumed values for the T_1/T_2 of water protons and the MT rate (22, 29, 30).

Mean PSR (mPSR) and mean T_2^M (m T_2^M) values for FG tissue were calculated for each scanning session for each patient by averaging the PSR values within the corresponding

VOI. PSR values greater than 30% were considered nonphysiological, and voxels exceeding that threshold were excluded from the analysis. These voxels were located primarily at tissue boundaries, where partial-volume effects may lead to erroneous fit values.

Statistical analyses were performed using the statistical toolbox in MATLAB 2007b (The MathWorks, Natick, Massachusetts). Previously published methods (31) based upon the work outlined by Galbraith et al. (32) were used to assess the reproducibility of mPSR measurements in the FG tissue of healthy controls. For each volunteer, the difference, d , between the measurement of mPSR from the first scanning session (mPSR₁) and mPSR from the second scanning session (mPSR₂) was calculated: $d = \text{mPSR}_2 - \text{mPSR}_1$. A Kendall's tau test was performed to ensure that the measurement error was not correlated with the mean, and the following statistical measurements of reproducibility were then computed: the 95% confidence interval (CI), the root-mean-squared deviation, the within-subject standard deviation, and the repeatability value (r).

An additional Kendall's tau test was performed to test for correlation between the average of the mPSR values and age, as it is known that breast tissue composition changes with age (33). Changes in T_2^M with treatment response are not expected, as it has been shown that T_2^M values are similar in both healthy and diseased tissues (29, 34); therefore, repeatability measures were not performed for the mT_2^M values.

RESULTS

Representative images from a single volunteer are shown in Figure 1. The saturated images (Figure 1A) and the reference image (Figure 1B) show robust fat suppression. The corresponding PSR map is shown as an overlay on the reference image (Figure 1C), showing a distribution of PSR values within the FG tissue. A map of the standard deviation of the fitted PSR values is also shown (Figure 1C) to provide an example of the estimated error in the nonlinear fit. Values of mT_2^M and mPSR for each scanning session and the difference, d , between the 2 mPSR values are listed in Table 1. The value of mT_2^M ranged from 2.7 to 3.9 μs and 2.6 to 10.3 μs for scans 1 and 2, respectively. The value of mPSR₁ ranged from 10.4% to 16.7%, the value of mPSR₂ ranged from 9.5% to 16.7%, and the absolute value of d ranged from 0.1% to 2.1%. PSR₁ and PSR₂ maps for the best ($|d| = 0.1\%$), average ($|d| = 0.9\%$), and the worst ($|d| = 2.1\%$) cases are shown in Figure 2. Histograms of PSR values for the individual voxels in the VOIs are plotted by the scan session in Figure 3. There was no significant correlation between the average of the 2 mPSR values and age (Kendall's tau, $P = .273$), as can be seen upon visual inspection of Figure 3.

There was no significant dependence of d on the mean value of the 2 measurements (Kendall's tau, $P = .165$). The values of d are plotted against the mean of mPSR₁ and mPSR₂ for each subject in the Bland–Altman plot as shown in Figure 4. The mean difference for all volunteers was -0.2% , which was not significantly different from 0 (t -test, $P = .543$). The 95% CI for the mean difference was $\pm 0.75\%$, root-mean-squared deviation was 1.09%, within-subject standard deviation was 0.77%, and repeatability value (r) was 2.39%.

DISCUSSION

To the best of our knowledge, this is the first report on PSR measurements of FG tissue in the breast in vivo. This study shows that the PSR of healthy FG tissue can be reliably measured using the sequence protocols and analysis pipelines described herein. Of particular note, robust fat suppression was achieved via a water-selective excitation pulse, minimizing the potential influence of fat on PSR values in the breast tissue; the semiautomated VOI selection algorithm was reliable across scan sessions; and the sequence can be performed in a clinically feasible scan time. The 95% CI for the mean difference was $\pm 0.75\%$, meaning that a change in mPSR greater than $\pm 0.75\%$ would exceed the expected measurement variability for a group of 11 patients. The repeatability value, r , was 2.39%, meaning that a change in PSR greater than $\pm 2.39\%$ would exceed the expected measurement variability for an individual. The relatively small interscan variability observed in this small cohort supports continued investigation into the use of PSR measurements in future longitudinal studies of breast cancer progression and/or treatment response.

Currently, there is a paucity of data on MT imaging of the breast in the literature. Santyr et al. (35) performed in vitro studies to assess the MT rates between solid- and liquid-like pools in different agar gels and excised FG specimens. These data, in combination with a theoretical MT model, were used to optimize an MT sequence appropriate for in vivo imaging. They showed that their technique could result in 40%–50% decrease in FG tissue signal, thereby making lesion visualization easier. Based on these data, in vivo MT imaging of the breast was first implemented to simply improve visualization of tissue enhancement after the injection of a standard gadolinium-based contrast agent (36, 37). Pierce et al. (36) showed a 30% reduction in signal with MT-weighting in 2 volunteers and noted improved tumor enhancement in patients with a variety of breast pathologies. Schreiber et al. (37) noted improved visualization of tissue enhancement in MT-weighted images after the injection of a standard gadolinium-based contrast agent. Callicott et al. (38) assessed T_1 and MT properties on breast tissue samples ex vivo. Although these MT methods were able to provide greater discrimination between lesions and the surrounding normal tissue, they were unable to reliably separate benign from malignant neoplasms. In contrast to these more qualitative approaches, Bonini et al. (11) and Heller et al. (12) were able to separate benign and malignant breast lesions by showing a significant reduction of MTR values in malignant cases. Bonini et al. (11) hypothesized that these findings were because of increased proteolytic activity and/or decreased activity of enzyme inhibitors in cancer, both of which may act to reduce the available macromolecular pool. However, those studies (like ours) were not designed to elucidate the underlying biochemical processes resulting in measured changes.

Decreased PSR values have been reported in gliomas in animal models (19, 20, 39), perhaps because of the increased water content within the tumor. Tozer et al. (40) reported reduced macromolecular pool fraction in human gliomas compared with normal-appearing white matter. Thus, given these previously published reports and the data presented here, future qMT-MRI studies designed to study the effects of various biophysical processes in breast cancer on PSR measurements are warranted.

The application of qMT-MRI to cancer imaging, in general, and to the current study is not without its limitations. The entire macromolecular pool affects measured PSR values, making it impossible to correlate changes observed in PSR with changes in the concentration of specific glycoproteins, and changes in PSR values are also affected by changes in water content (eg, inflammation or edema). In addition, the relationship between FG composition and PSR measurements is currently not fully understood. Although FG composition is known to change with age and menstrual status, age does not appear to affect the repeatability measures in this study, as seen in Figure 3 and Table 1; furthermore, Clendenen et al. (41) recently reported that FG MTR values do not vary significantly across the different phases of the menstrual cycle. Variation due to the menstrual cycle was controlled for in the present work by scanning each volunteer within the same scan session, and this may not be an issue in the clinical setting as patients often experience chemotherapy-induced amenorrhea (42).

Another potential limitation of qMT-MRI is that accurate estimation of model parameters requires the acquisition of several image volumes at multiple offset frequencies and/or powers, potentially making the scan prohibitively long. Two ways to overcome this challenge are to reduce the number of image acquisitions by designing optimal sampling strategies (43) and to fix certain model parameters in the fitting procedure (20). As an initial attempt, we selected a combination of 4 offset frequencies and 2 powers for a total of 8 MT-weighted image volumes to reduce the acquisition time and allow for respiratory gating. We also chose to fix the T_1/T_2 of water protons and the MT rate to values previously reported for muscle (29); however, future work may include modeling to estimate the bias introduced by these parameter assumptions.

The pulsed saturation technique used here requires additional image acquisitions (T_1 , B_1^+ , and B_0), potentially increasing the total scan time for an imaging session (18, 22, 44); however, a pulsed saturation technique was chosen for this study for 2 reasons. First, it is the most practical for clinical application because it can be applied within the hardware constraints of clinical systems and within patient safety limits for RF power deposition. Second, the protocol for the clinical trial (5), in which we propose to add qMT imaging, currently includes T_1 and B_1^+ acquisitions for DCE-MRI analysis, meaning the only additional scan time is for the B_0 mapping, which takes less than 10 seconds.

The dependence of the pulsed saturation technique on 3 additional image acquisitions also raises the concern that each additional acquisition might introduce bias into PSR estimation. However, the methods applied in this study attempt to mitigate those effects. First, the lowest offset frequency applied in this study was 1 kHz; therefore, errors in B_0 on the order of 50 Hz (45) would result in negligible errors in PSR (simulations not shown). Second, PSR measurements are effectively insensitive to B_1^+ error when the B_1^+ map is used for both the correction of the T_1 mapping and the qMT analysis (46), as was done in this effort. Finally, PSR bias scales linearly with errors in $1/T_1$, and the T_1 mapping method used in this work, which included B_1 correction, has been shown to produce reliable results (47).

In conclusion, the results of this study demonstrate the feasibility of performing qMT-MRI of the breast in healthy controls using a pulsed saturation technique. PSR measurements of

the FG tissue estimated with a 2-pool model were reproducible over 2 scan sessions. Future work includes applying the technique in an ongoing longitudinal, multiparametric study of treatment assessment in breast cancer (5).

Acknowledgments

We thank the National Institutes of Health for funding through NCATS UL1 TR000445, NCI U01CA174706, NCI 1U01CA142565, NCI 1P50 098131, NIH EB013659, and NIH P30 CA68485, and CPRIT RR160005. Thomas E. Yankeelov is a CPRIT Scholar of Cancer Research. We offer our sincere thanks to the women who participated in our study. We thank Ms. Kristen George-Durrett, Ms. Clair Kurtenbach, Ms. Leslie McIntosh, and Mr. Christopher Thompson for expert technical assistance. We thank the Kleberg Foundation for the generous support of our imaging program.

Abbreviations

MRI	Magnetic resonance imaging
DCE-MRI	Dynamic contrast-enhanced MRI
ECM	extracellular matrix
MT-MRI	magnetization transfer MRI
MT	magnetization transfer
MTR	MT ratio
qMT	quantitative MT
FOV	field of view
FG	fibroglandular
VOI	volume of interest
mPSR	mean PSR
mT₂M	mean T ₂ M
mPSR₁	mPSR from the first scanning session
mPSR₂	mPSR from the second scanning session
CI	confidence interval
TE	echo time
TR	repetition time
PSR	pool size ratio
RF	radiofrequency

References

1. Hanahan D, Weinberg RA. Hallmarks of cancer: the next generation. *Cell*. 2011; 144(5):646–674. [PubMed: 21376230]
2. Sawyers C. Targeted cancer therapy. *Nature*. 2004; 432(7015):294–297. [PubMed: 15549090]
3. Yankeelov TE, Gore JC. Dynamic contrast enhanced magnetic resonance imaging in oncology: theory, data acquisition, analysis, and examples. *Curr Med Imaging Rev*. 2009; 3(2):91–107. [PubMed: 19829742]
4. Padhani AR, Liu G, Mu-Koh D, Chenevert TL, Thoeny HC, Takahara T, Dzik-Jurasz A, Ross BD, Van Cauteren M, Collins D, Hammoud DA, Rustin GJ, Taouli B, Choyke PL. Diffusion-weighted magnetic resonance imaging as a cancer bio-marker: consensus and recommendations. *Neoplasia*. 2009; 11(2):102–125. [PubMed: 19186405]
5. Li X, Abramson RG, Arlinghaus LR, Kang H, Chakravarthy AB, Abramson VG, Farley J, Mayer IA, Kelley MC, Meszoely IM, Means-Powell J, Grau AM, Sanders M, Yankeelov TE. Multiparametric magnetic resonance imaging for predicting pathological response after the first cycle of neoadjuvant chemotherapy in breast cancer. *Invest Radiol*. 2015; 50(4):195–204. [PubMed: 25360603]
6. Egeblad M, Nakasone ES, Werb Z. Tumors as organs: complex tissues that interface with the entire organism. *Dev Cell*. 2010; 18(6):884–901. [PubMed: 20627072]
7. Narunsky L, Oren R, Bochner F, Neeman M. Imaging aspects of the tumor stroma with therapeutic implications. *Pharmacol Ther*. 2014; 141(2):192–208. [PubMed: 24134903]
8. Nelson CM, Bissell MJ. Of extracellular matrix, scaffolds, and signaling: tissue architecture regulates development, homeostasis, and cancer. *Annu Rev Cell Dev Biol*. 2006; 22(1):287–309. [PubMed: 16824016]
9. Stetler-Stevenson WG, Aznavoorian S, Liotta LA. Tumor-cell interactions with the extracellular-matrix during invasion and metastasis. *Annu Rev Cell Biol*. 1993; 9(1):541–573. [PubMed: 8280471]
10. Wolff SD, Balaban RS. Magnetization transfer contrast (MTC) and tissue water proton relaxation in vivo. *Magn Reson Med*. 1989; 10(1):135–144. [PubMed: 2547135]
11. Bonini RH, Zeotti D, Saraiva LA, Trad CS, Filho JM, Carrara HH, de Andrade JM, Santos AC, Muglia VF. Magnetization transfer ratio as a predictor of malignancy in breast lesions: preliminary results. *Magn Reson Med*. 2008; 59(5):1030–1034. [PubMed: 18429009]
12. Heller SL, Moy L, Lavianlivi S, Moccaldi M, Kim S. Differentiation of malignant and benign breast lesions using magnetization transfer imaging and dynamic contrast-enhanced MRI. *J Magn Reson Imaging*. 2013; 37(1):138–145. [PubMed: 23097239]
13. Kakkad SM, Solaiyappan M, O'Rourke B, Stasinopoulos I, Ackerstaff E, Raman V, Bhujwala ZM, Glunde K. Hypoxic tumor microenvironments reduce collagen I fiber density. *Neoplasia*. 2010; 12(8):608–617. [PubMed: 20689755]
14. Rajan R, Esteva FJ, Symmans WF. Pathologic changes in breast cancer following neoadjuvant chemotherapy: implications for the assessment of response. *Clin Breast Cancer*. 2004; 5(3):235–238. [PubMed: 15335458]
15. Sahoo S, Lester SC. Pathology of breast carcinomas after neoadjuvant chemotherapy an overview with recommendations on specimen processing and reporting. *Arch Pathol Lab Med*. 2009; 133(4):633–642. [PubMed: 19391665]
16. Sneige N, Kemp B, Pusztai L, Asmar L, Hortobagyi GN. Chemotherapy-induced histologic changes in mastectomy specimens and their potential significance. *Breast*. 2001; 10(6):492–500. [PubMed: 14965629]
17. Henkelman RM, Huang XM, Xiang QS, Stanisz GJ, Swanson SD, Bronskill MJ. Quantitative interpretation of magnetization-transfer. *Magn Reson Med*. 1993; 29(6):759–766. [PubMed: 8350718]
18. Sled JG, Pike GB. Quantitative imaging of magnetization transfer exchange and relaxation properties in vivo using MRI. *Magn Reson Med*. 2001; 46(5):923–931. [PubMed: 11675644]

19. Xu J, Li K, Zu Z, Li X, Gochberg DF, Gore JC. Quantitative magnetization transfer imaging of rodent glioma using selective inversion recovery. *NMR Biomed.* 2014; 27(3):253–260. [PubMed: 24338993]
20. Underhill HR, Rostomily RC, Mikheev AM, Yuan C, Yarnykh VL. Fast bound pool fraction imaging of the in vivo rat brain: association with myelin content and validation in the C6 glioma model. *Neuroimage.* 2011; 54(3):2052–2065. [PubMed: 21029782]
21. Quesson B, Bouzier AK, Thiaudiere E, Delalande C, Merle M, Canioni P. Magnetization transfer fast imaging of implanted glioma in the rat brain at 4.7 T: interpretation using a binary spin-bath model. *J Magn Reson Imaging.* 1997; 7(6):1076–1083. [PubMed: 9400852]
22. Yarnykh VL. Pulsed Z-spectroscopic imaging of cross-relaxation parameters in tissues for human MRI: theory and clinical applications. *Magn Reson Med.* 2002; 47(5):929–939. [PubMed: 11979572]
23. Li W, Zhang Z, Nicolai J, Yang G-Y, Omary RA, Larson AC. Quantitative magnetization transfer MRI of desmoplasia in pancreatic ductal adenocarcinoma xenografts. *NMR Biomed.* 2013; 26(12):1688–1695. [PubMed: 23940016]
24. Yarnykh VL, Tartaglione EV, Ioannou GN. Fast macromolecular proton fraction mapping of the human liver in vivo for quantitative assessment of hepatic fibrosis. *NMR Biomed.* 2015; 28(12):1716–1725. [PubMed: 26503401]
25. Harris PA, Taylor R, Thielke R, Payne J, Gonzalez N, Conde JG. Research electronic data capture (REDCap)—a metadata-driven methodology and workflow process for providing translational research informatics support. *J Biomed Inform.* 2009; 42(2):377–381. [PubMed: 18929686]
26. Jankiewicz M, Gore JC, Grissom WA. Improved encoding pulses for Bloch-Siegert B1(+) mapping. *J Magn Reson.* 2013; 226:79–87. [PubMed: 23220183]
27. Dula AN, Arlinghaus LR, Dortch RD, Dewey BE, Whisenant JG, Ayers GD, Yankeelov TE, Smith SA. Amide proton transfer imaging of the breast at 3 T: establishing reproducibility and possible feasibility assessing chemotherapy response. *Magn Reson Med.* 2013; 70(1):216–224. [PubMed: 22907893]
28. Ramani A, Dalton C, Miller DH, Tofts PS, Barker GJ. Precise estimate of fundamental in-vivo MT parameters in human brain in clinically feasible times. *Magn Reson Imaging.* 2002; 20(10):721–731. [PubMed: 12591568]
29. Li K, Dortch RD, Kroop SF, Huston JW, Gochberg DF, Park JH, Damon BM. A rapid approach for quantitative magnetization transfer imaging in thigh muscles using the pulsed saturation method. *Magn Reson Imaging.* 2015; 33(6):709–717. [PubMed: 25839394]
30. Smith AK, Dortch RD, Dethrage LM, Smith SA. Rapid, high-resolution quantitative magnetization transfer MRI of the human spinal cord. *Neuroimage.* 2014; 95:106–116. [PubMed: 24632465]
31. Whisenant JG, Ayers GD, Loveless ME, Barnes SL, Colvin DC, Yankeelov TE. Assessing reproducibility of diffusion-weighted magnetic resonance imaging studies in a murine model of HER2+ breast cancer. *Magn Reson Imaging.* 2014; 32(3):245–249. [PubMed: 24433723]
32. Galbraith SM, Lodge MA, Taylor NJ, Rustin GJS, Bentzen S, Stirling JJ, Padhani AR. Reproducibility of dynamic contrast-enhanced MRI in human muscle and tumours: comparison of quantitative and semi-quantitative analysis. *NMR Biomed.* 2002; 15(2):132–142. [PubMed: 11870909]
33. Rutter CM, Mandelson MT, Laya MB, Seger DJ, Taplin S. Changes in breast density associated with initiation, discontinuation, and continuing use of hormone replacement therapy. *JAMA.* 2001; 285(2):171–176. [PubMed: 11176809]
34. Yarnykh VL, Yuan C. Cross-relaxation imaging reveals detailed anatomy of white matter fiber tracts in the human brain. *Neuroimage.* 2004; 23(1):409–424. [PubMed: 15325389]
35. Santyr GE, Kelcz F, Schneider E. Pulsed magnetization transfer contrast for MR imaging with application to breast. *J Magn Reson Imaging.* 1996; 6(1):203–212. [PubMed: 8851429]
36. Pierce WB, Harms SE, Flamig DP, Griffey RH, Evans WP, Hagans JE. 3-Dimensional gadolinium-enhanced MR imaging of the breast: pulse sequence with fat suppression and magnetization transfer contrast. *Work in progress. Radiology.* 1991; 181(3):757–763. [PubMed: 1947093]

37. Schreiber WG, Brix G, Knopp MV, Hess T, Lorenz WJ. Improved visualization of breast lesions with gadolinium-enhanced magnetization transfer MR imaging. *Magn Reson Med*. 1996; 35(6): 861–869. [PubMed: 8744014]
38. Callicott C, Thomas JM, Goode AW. The magnetization transfer characteristics of human breast tissues: an in vitro NMR study. *Phys Med Biol*. 1999; 44(5):1147–1154. [PubMed: 10368008]
39. Li K, Li H, Zhang XY, Stokes AM, Jiang X, Kang H, Quarles CC, Zu Z, Gochberg DF, Gore JC, Xu J. Influence of water compartmentation and heterogeneous relaxation on quantitative magnetization transfer imaging in rodent brain tumors. *Magn Reson Med*. 2016; 76(2):635–644. [PubMed: 26375875]
40. Tozer DJ, Rees JH, Benton CE, Waldman AD, Jager HR, Tofts PS. Quantitative magnetisation transfer imaging in glioma: preliminary results. *NMR Biomed*. 2011; 24(5):492–498. [PubMed: 20960580]
41. Clendenen TV, Kim S, Moy L, Wan L, Rusinek H, Stanczyk FZ, Pike MC, Zeleniuch-Jacquotte A. Magnetic resonance imaging (MRI) of hormone-induced breast changes in young premenopausal women. *Magn Reson Imaging*. 2013; 31(1):1–9. [PubMed: 22898693]
42. Rose DP, Davis TE. Ovarian function in patients receiving adjuvant chemotherapy for breast cancer. *Lancet*. 1977; 309(8023):1174–1176.
43. Cercignani M, Alexander DC. Optimal acquisition schemes for in vivo quantitative magnetization transfer MRI. *Magn Reson Med*. 2006; 56(4):803–810. [PubMed: 16902982]
44. Sled JG, Pike GB. Quantitative interpretation of magnetization transfer in spoiled gradient echo MRI sequences. *J Magn Reson*. 2000; 145(1):24–36. [PubMed: 10873494]
45. Jordan CD, Daniel BL, Koch KM, Yu H, Conolly S, Hargreaves BA. Subject-specific models of susceptibility-induced B(0) field variations in breast MRI. *J Magn Reson Imaging*. 2013; 37(1): 227–232. [PubMed: 22865658]
46. Boudreau, M.; Stikov, N.; Pike, GB. B1-Sensitivity Analysis of qMT. Proceedings of the 23rd Annual Meeting of ISMRM; Toronto, Ontario, Canada. 2015. Abstract 1741
47. Whisenant JG, Dortch RD, Grissom WA, Kang H, Arlinghaus LR, Yankeelov TE. Bloch-Siegert B1-mapping Improves Accuracy and Precision of Longitudinal Relaxation Measurements in the Breast at 3T. *Tomography*. In press.

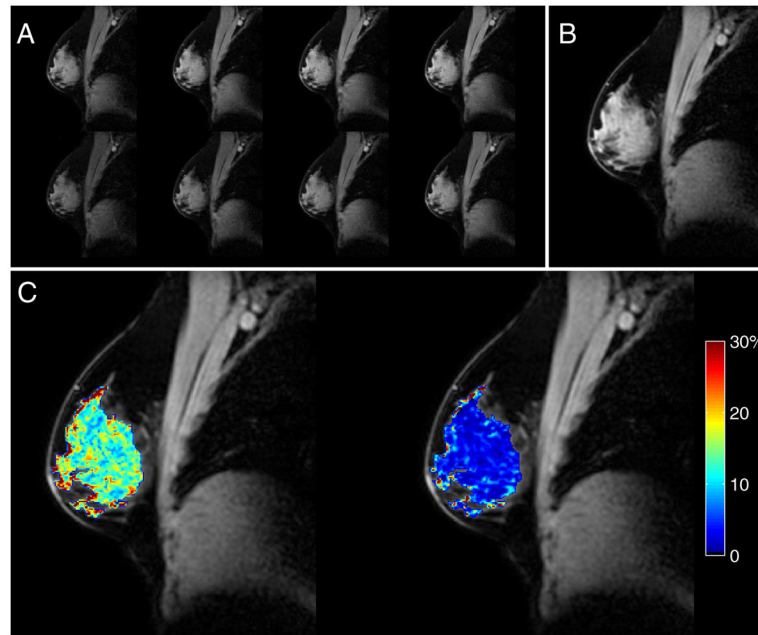


Figure 1. Quantitative magnetization transfer magnetic resonance imaging (qMT-MRI) data are shown for a typical subject (age = 26 years): the 8 magnetization transfer (MT)-weighted images, with pulse angles of 500° (top row) and 800° (bottom row) and offsets of 1, 2, 4, and 8 kHz (left to right) (A); the normalization image (offset frequency = 100 kHz and pulse angle = 800°) (B); and the corresponding pool size ratio (PSR) map (left) and map of the standard deviation (SD) of the PSR values (right) (C) calculated during the fitting process. The mPSR \pm SD for this subject and scanning session was 14.5% \pm 5.9%.

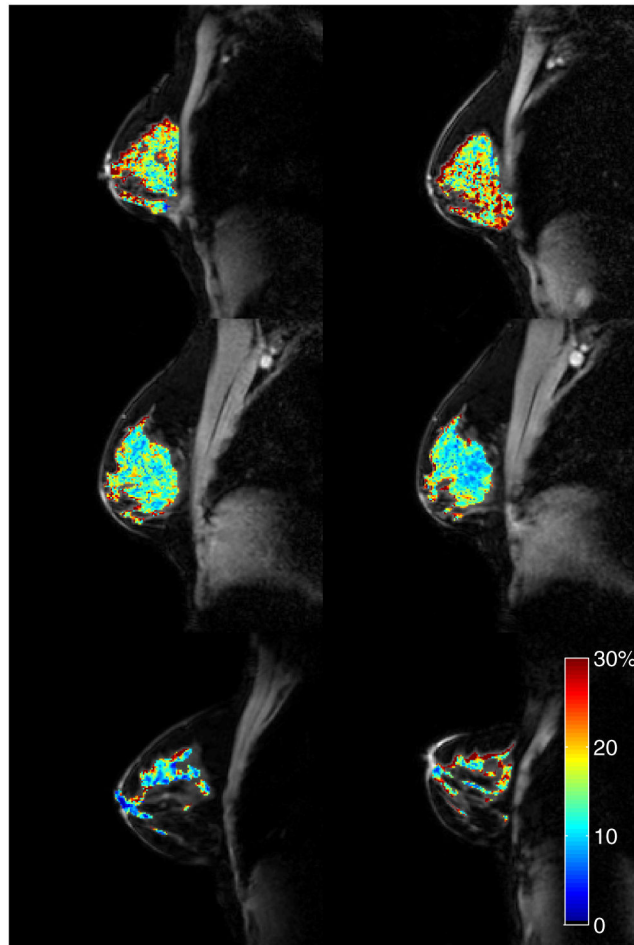


Figure 2. Reproducibility in healthy controls. From top to bottom, each row displays examples of the best ($|d| = 0.1\%$), average ($|d| = 0.9\%$), and the worst ($|d| = 2.1\%$) cases, based on the absolute value of the difference ($|d|$) between the mean fibroglandular (FG) PSR values from scan 1 (left column) to scan 2 (right column). The PSR maps are displayed as overlays on the corresponding normalization images.

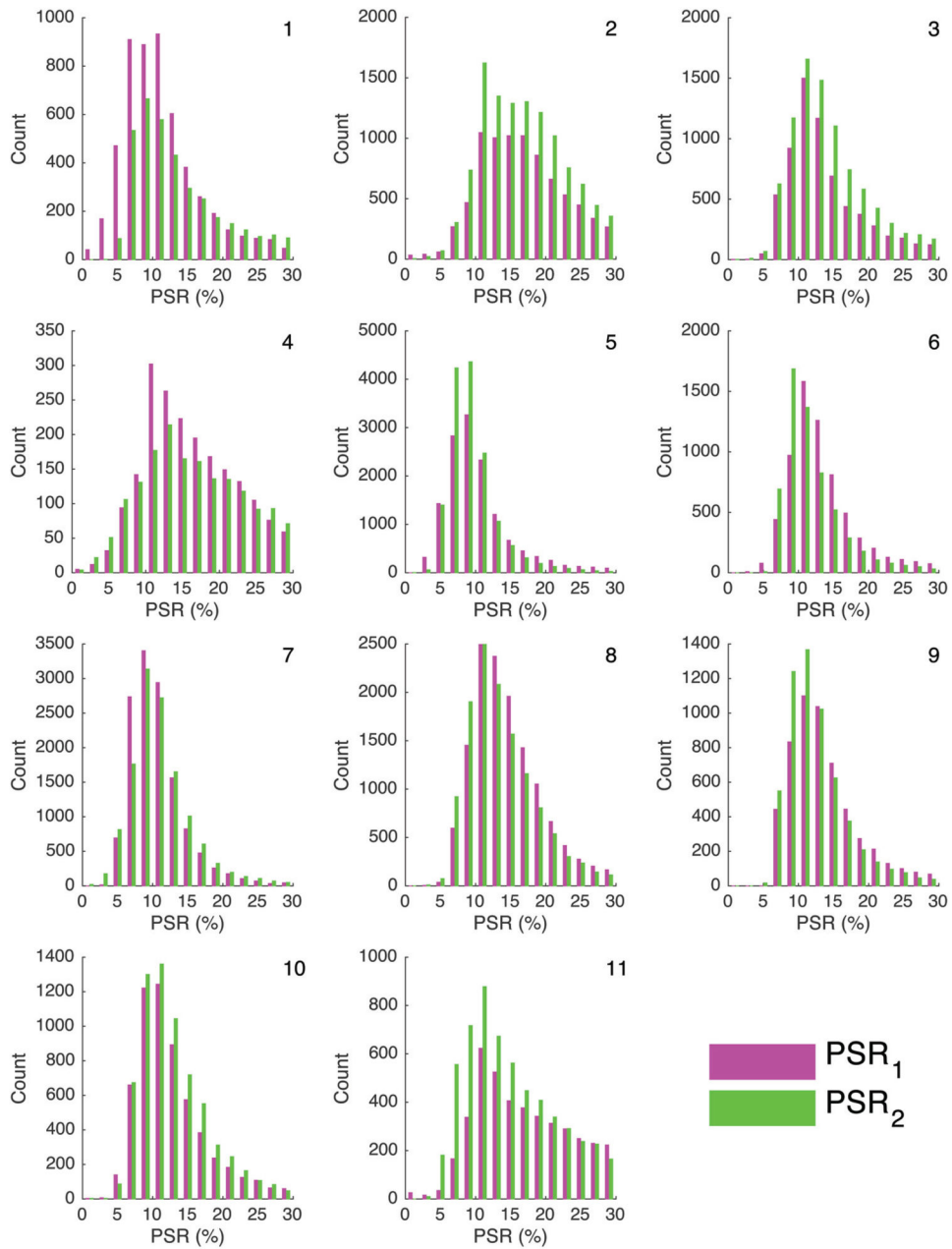


Figure 3. Histograms of PSR values for all FG voxels are plotted by scan session (magenta: first scan, green: second scan) for each of the 11 subjects.

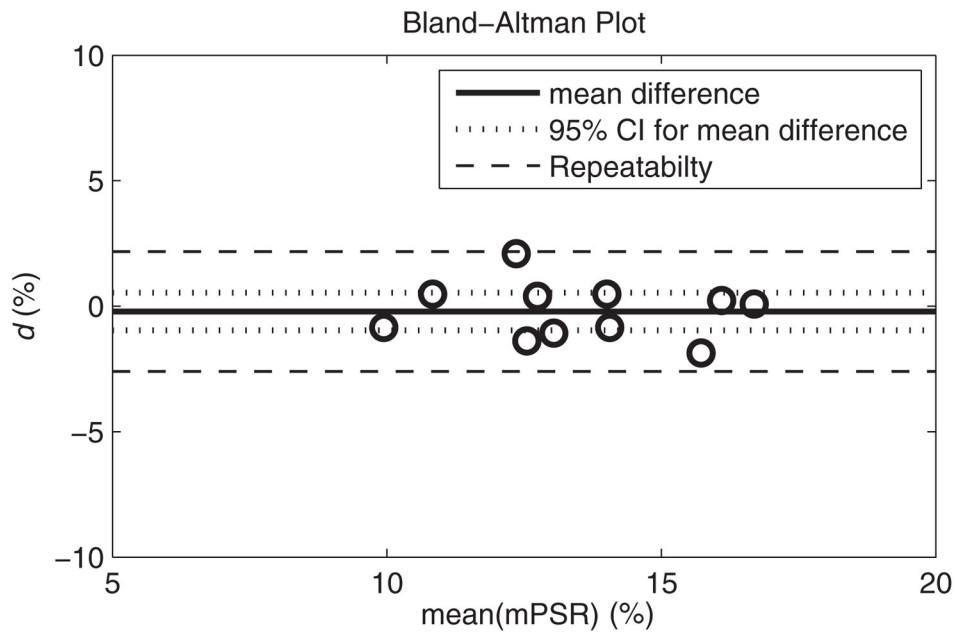


Figure 4. Difference (d) between mean PSR (mPSR) values in the FG tissue from 2 scanning sessions plotted against the average of the 2 FG mPSR values for each volunteer. The overall mean difference between scans (solid line) for all 11 subjects was not significantly different from 0 ($P = .543$). The 95% confidence interval (CI) for the group (dotted line) was 0.75, and it represents the level of change that would be significant for a group of 11 subjects. The repeatability (dashed line) was 2.39, and it represents the level of change that would be significant in an individual.

Table 1

Age, T_2M , and PSR Data

Subject No.	Age	$mT_2M(\mu s)$		mPSR (%)		d
		Scan 1	Scan 2	Scan 1	Scan 2	
1	42	3.6	3.4	11.3	13.4	2.1
2	51	3.1	3.2	16.7	16.7	0.1
3	29	3.0	2.9	13.8	14.2	0.5
4	54	3.9	10.3	16.0	16.2	0.2
5	36	2.8	2.9	10.4	9.5	-0.9
6	27	2.9	3.1	13.3	11.9	-1.4
7	25	3.1	2.6	10.6	11.1	0.5
8	26	3.0	3.1	14.5	13.6	-0.9
9	36	2.9	3.3	13.6	12.5	-1.1
10	27	2.7	2.9	12.6	12.9	0.4
11	33	3.9	5.0	16.7	14.8	-1.9